RESEARCH ARTICLE

From tunable core-shell nanoparticles to plasmonic drawbridges: Active control of nanoparticle optical properties

Chad P. Byers,[1,2] Hui Zhang,[3] Dayne F. Swearer,[2] Mustafa Yorulmaz,[2] Benjamin S. Hoener,[2] Da Huang,[2] Anneli Hoggard,[2] Wei-Shun Chang,[2] Paul Mulvaney,[4] Emilie Ringe,[2,5] Naomi J. Halas,[1,2,3,5,6] Peter Nordlander,[1,3,5,6] Stephan Link,[1,2,6] Christy F. Landes[1,2,6]*

The optical properties of metallic nanoparticles are highly sensitive to interparticle distance, giving rise to dramatic but frequently irreversible color changes. By electrochemical modification of individual nanoparticles and nanoparticle pairs, we induced equally dramatic, yet reversible, changes in their optical properties. We achieved plasmon tuning by oxidation-reduction chemistry of Ag-AgCl shells on the surfaces of both individual and strongly coupled Au nanoparticle pairs, resulting in extreme but reversible changes in scattering line shape. We demonstrated reversible formation of the charge transfer plasmon mode by switching between capacitive and conductive electronic coupling mechanisms. Dynamic single-particle spectroelectrochemistry also gave an insight into the reaction kinetics and evolution of the charge transfer plasmon mode in an electrochemically tunable structure. Our study represents a highly useful approach to the precise tuning of the morphology of narrow interparticle gaps and will be of value for controlling and activating a range of properties such as extreme plasmon modulation, nanoscopic plasmon switching, and subnanometer tunable gap applications.

INTRODUCTION

Active control of the optical and electronic properties of nanoparticles is critical for many future technological applications, yet remains largely elusive. Optical tunability of metallic nanoparticles can be achieved by exploiting the sensitivity of the localized surface plasmon. Researchers in pursuit of in situ active control have used electronic (*1, 2*), chemical (*3*), and electrochemical (*4–9*) approaches. Recent electrochemical efforts have resulted in either small reversible modulations (*7, 8*) or large irreversible plasmon shifts (*10, 11*). One strategy toward achieving larger plasmon resonance shifts is tuning the plasmon coupling strength between adjacent nanostructures. Modest tunability of the capacitive coupling between nanoparticles was achieved with lithographically prepared dimers on a stretchable elastomeric substrate (*12, 13*). For strongly coupled nanoparticles (gaps <1 nm), quantum effects strongly influence the optical response (*14–18*), and electron tunneling conductance between nanostructures depends exponentially on the gap width (*18–20*). If the gap is further decreased until the structures are within tunneling contact, optical-frequency electric currents can flow through the entire joined structure, resulting in the emergence of new plasmon modes (*14–17, 21*). Transitions from capacitive to conductive coupling produce enormous spectral changes, but so far all in situ fully nanoscopic methods have been irreversible (*22–24*). To date, reversible tuning between capacitive and conductive plasmon coupling has only been achieved for one nanostructure at a time using nanopositioners (*14*). Significant challenges still remain for active nanophotonic control over a broad optical range.

In this report, we demonstrate reversible, active plasmon control through electrochemical reduction and chloridation of Ag metal on both isolated Au nanoparticles and strongly coupled Au nanoparticle dimers. Large changes in nanoparticle optical spectra are typically irreversible, but here we demonstrate a simple and robust chemical mechanism that allows large reversible changes in nanoparticle optical properties. We tune the optical and electronic properties by electrochemically controlling the nanostructure morphology, chemical composition, electronic coupling strength, and, ultimately, fundamental coupling mechanism. We initially demonstrate reversible tuning of the localized surface plasmon resonance of individual core-shell Au/Ag nanoparticles through Ag redox electrochemistry, the fundamentals of which have only recently been demonstrated (*10, 25*) (Au/Ag denotes gold core with silver shell). Here, the well-known Ag-AgCl redox chemistry (*26*) allows for reversible resonance energy shifts and intensity modulation that are one and three orders of magnitude larger than charge density tuning, respectively. We then reversibly tune the hybridized bonding plasmon mode of strongly coupled individual Au/Ag nanoparticle dimers. Finally, by electrochemically bridging the interparticle gap, we demonstrate fully reversible transitions between capacitive and conductive coupling regimes, as evidenced by the dynamic evolution of the charge transfer plasmon (CTP) mode. Our study represents the first demonstration of active switching between these two coupling regimes on individual nanoparticle pairs in a completely nanoscopic system, as well as the first reported switchable and tunable CTP. These advances will provide a valuable tool for precise gap control and plasmon tuning, which are of importance for both the development of active plasmonic devices such as switches and modulators, as emphasized here, and, more broadly, for the emerging field of quantum plasmonics, which relies on precise gap control.

RESULTS

Reversible electrochemical redox tuning of Au/Ag nanoparticles

We used single-nanoparticle spectroelectrochemistry (*7, 10*), specifically the redox chemistry of Ag/AgCl (*27*), to actively tune the intensity,

[1]Smalley-Curl Institute Applied Physics Program, Rice University, Houston, TX 77005, USA. [2]Department of Chemistry, Rice University, Houston, TX 77005, USA. [3]Department of Physics and Astronomy, Rice University, Houston, TX 77005, USA. [4]School of Chemistry and Bio21 Institute, University of Melbourne, Parkville, Victoria 3010, Australia. [5]Materials Science and Nanoengineering, Rice University, Houston, TX 77005, USA. [6]Department of Electrical and Computer Engineering, Rice University, Houston, TX 77005, USA.
*Corresponding author. E-mail: cflandes@rice.edu

Byers *et al. Sci. Adv.* 2015;1:e1500988   4 December 2015

1 of 9

spectral line shape, and resonance energy of single Au/Ag nanoparticles (Fig. 1). Ag chloro-complex ions were produced anodically from an Ag/AgCl counter electrode and reduced on cathodically polarized bare Au 50-nm spherical nanoparticles to form Au/Ag core-shell nanoparticles in a transparent spectroelectrochemical cell (28–31). The light-scattering properties of individual Au/Ag nanoparticles were reversibly tuned by repeatedly interconverting the shell between Ag and AgCl by electrochemical potential cycling (Fig. 1A). High-angle annular dark-field scanning transmission electron microscopy (HAADF-STEM) and energy-dispersive x-ray spectroscopy (EDS) elemental maps showed the clear core-shell structure of the Au/Ag nanoparticles (Fig. 1B and fig. S1).

Multiple series of scattering spectra of individual Au/Ag nanoparticles were collected during cyclic voltammetry experiments. Scattering spectra displayed well-defined potential-dependent plasmon resonance energy (E), full width at half maximum (Γ), and intensity (I) (Fig. 1C). Others have shown recently that, under specific electrolyte conditions, electrochemical oxidation of pure Ag nanoparticles resulted in complete oxidation and dissolution of the nanoparticles (28, 32). In contrast, the use of the core-shell geometry and the inclusion of chloride ions in our system allowed for reversible tuning between two stable states with well-defined optical properties. Here, the different oxidation potentials of Ag and Au allowed us to electrochemically oxidize the Au/Ag nanoparticle to Au/AgCl. Mean changes in E, Γ, and I were tracked as a function of potential over five cycles (Fig. 1C) under three different cell conditions: a bare Au nanoparticle in a cell with Pt reference and counter electrodes, thus containing no Ag (gray); an Au nanoparticle in the presence of a low-concentration Ag chloro-complex solution (green); and a higher-concentration Ag chloro-complex solution (blue), achieved by using a Ag counter electrode and by tuning the Cl⁻ electrolyte concentration. In the control sample containing no Ag, E, Γ, and I showed small linear shifts with applied potential due to electrochemically induced charge density tuning, as previously reported (7, 8). In contrast, redox tuning of the Ag shells of Au/Ag nanoparticles resulted in nonlinear plasmon resonance shifts. At a low Cl⁻ concentration and therefore low Ag chloro-complex concentration, redox tuning induced much larger shifts than charge density tuning alone. Increasing Cl⁻ concentration by a factor of 10 (to 1 M) raises the Ag chloro-complex solubility nearly 30-fold (26), which led to much larger shifts because of increased Ag shell thickness. Therefore, the extent of reversible optical tuning is directly controllable by means of the salt concentration.

At 1 M NaCl and negative applied potentials where AgCl is reduced to Ag, we observed spectral blue shifts of 15 meV followed by large red shifts of 50 meV (Fig. 1C, blue lines). This complex response is the product of three competing mechanisms and their impacts on the nanoparticle plasmon: (i) In the AgCl shell case, the local refractive index seen by the nanoparticle plasmon is that of the AgCl dielectric shell. Once the shell is converted into Ag, the surface plasmon resides on the outer Ag surface and the medium refractive index is that of the surrounding electrolyte, resulting in a decrease from n_{AgCl} (s) = 2.02 (33, 34) to $n_{electrolyte}$ = 1.34. The decrease in refractive index causes E and Γ to increase and I to decrease. (ii) A change in nanoparticle optical properties occurs as the dielectric AgCl is replaced by Ag metal that supports plasmon resonances in the visible. This effect causes E and I to increase and Γ to decrease. (iii) In the AgCl shell case, the surface plasmon resides on the Au core surface; but in the Ag shell case, the entire Au/Ag nanoparticle supports the plasmon oscillation (fig. S2). This increase in effective size and the elimination of the dielectric shell cause E to decrease and Γ and I to increase. The opposite responses are expected when the Ag shell is converted back into AgCl. The first
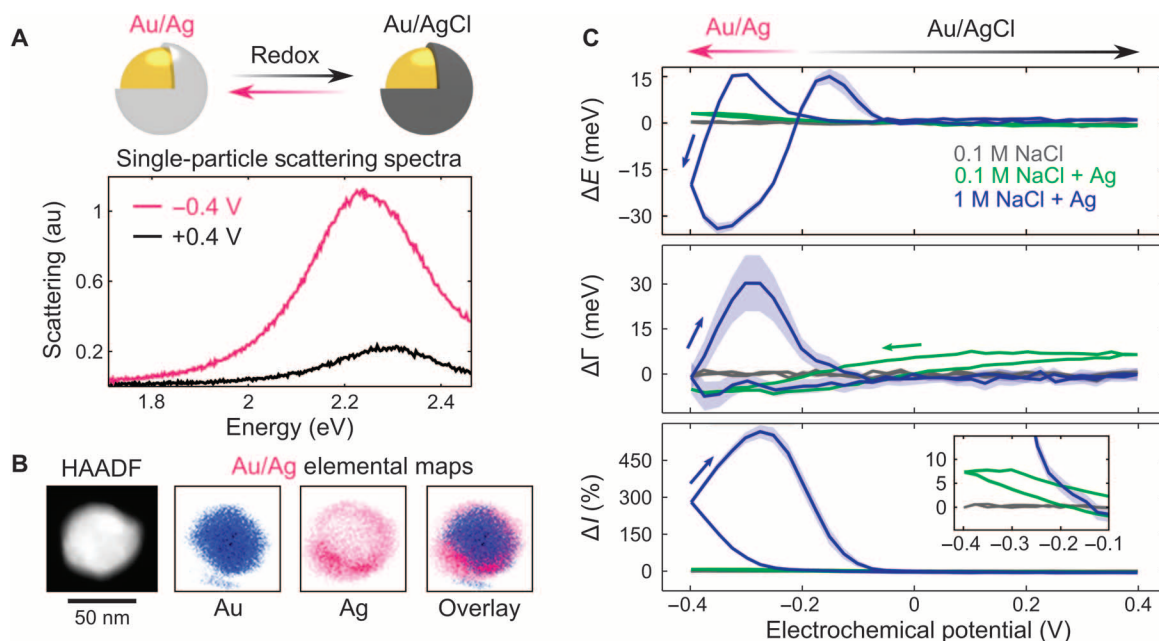

Fig. 1. Reversible redox tuning of Au/Ag nanoparticles. (**A**) Nanoparticle shells were reversibly switched between Ag and AgCl using redox electrochemistry. The optical response to redox tuning was measured using single-particle spectroscopy under electrochemical potential control. (**B**) HAADF-STEM and EDS elemental maps of a single Au/Ag nanoparticle show clear core-shell geometry. (**C**) Mean response over five cycles of changes in resonance energy (ΔE), full width at half maximum ($\Delta\Gamma$), and intensity (ΔI) as a function of applied potential under different electrolyte conditions. (Inset) Small-intensity response for control and thin-shell cases. Shaded bounds indicate standard error. au, arbitrary units.

two mechanisms cause an initial blue shift; but as the Ag shell grows thicker, mechanism (iii) causes a net red shift and increases in Γ and I. In this system, single-particle plasmon spectroelectrochemistry (our method) during cyclic voltammetry is crucial in analyzing nanoparticle plasmonic responses to chemical processes. Unlike cyclic voltammetry, which measures the electric current passed to and from the entire working electrode, the potential-dependent plasmon resonances report on changes in the composition, charge, damping, and scattering cross section of individual nanoparticles.

Redox tuning of strongly coupled nanoparticle dimers

The Ag-AgCl redox spectroelectrochemistry was extended to individual strongly coupled plasmonic dimers to take advantage of nonlinear gap effects (Fig. 2). Dimers nominally consisting of Au nanoparticles 50 nm in diameter were chemically assembled using a nonspecific aggregation method and were enriched through electrophoretic separation (35, 36). Transmission electron microscopy (TEM) micrographs revealed that Au dimers had gap widths ranging from 1 to 5 nm and

mean core diameter of 45.5 nm, with significant size and shape dispersity (fig. S3).

We hypothesized that the effective gap width of the dimers could be tuned by depositing a thin switchable Ag shell. Full-wave simulations using the finite element method (FEM) showed that for Ag shells, the shell itself would dominate the optical response (Fig. 2A, left). However, when switched to AgCl, the Au cores should dominate (Fig. 2A, right) (charge density maps generated at a plasmon resonance of 1.88 eV; additional details of FEM simulations can be found in Supplementary Materials). Charge primarily resides on the metallic Ag shells under electrochemically reducing conditions and on the Au cores under oxidizing conditions, leading to a change in effective gap width. The strong electric field enhancement caused by the cores also causes a visible polarization in the AgCl shell in the gap region (Fig. 2A, bottom right). The nonlinear response to gap width change allows significant tuning of the longitudinal bonding (LB) dipolar plasmon mode (Fig. 2B). Because the transverse (T) mode weakly depends on gap width, predicted changes are smaller (fig. S4).
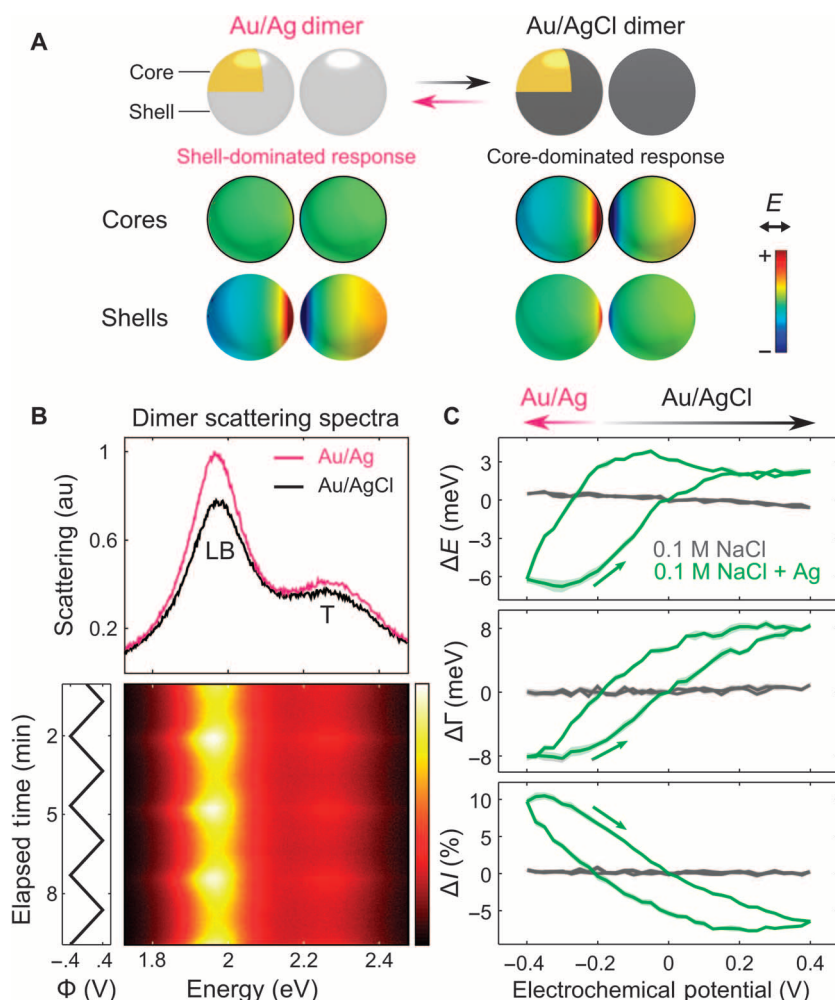

Fig. 2. Dimer surface plasmon response to reversible electrochemical redox tuning. (**A**) Thin shells on strongly coupled Au dimers were reversibly switched between Ag and AgCl. Charge density maps of the core and shell surfaces show that the optical response is dominated by Au cores in Au/AgCl dimers, but by Ag shells in Au/Ag dimers. Maps were generated at 1.88 eV. (**B**) Scattering spectra during dynamic potential control show clear modulation with changes in shell composition. (**C**) Mean LB mode ΔE, $\Delta \Gamma$, and ΔI over five cycles as a function of applied potential. Shaded bounds indicate standard error (smaller than linewidth at most points).

The spectral response of an individual dimer's LB mode to Ag shell redox tuning is compared to a bare Au dimer control (Fig. 2C). In the absence of a redox-tunable Ag shell, E, Γ, and I decreased linearly with increasing potential. These results are consistent with the single-nanoparticle charge density tuning described in Fig. 1C (gray lines; 0.1 M NaCl) and reported previously (7). In stark contrast, the plasmonic response to redox tuning of Au/Ag dimers exhibited a large hysteretic response, with E strongly decreasing with increasingly negative potentials. This inverted trend is easily explained within the plasmon ruler model (37); as the gap between metallic surfaces decreases when AgCl salt shells are reduced to metallic Ag shells, capacitive plasmon coupling strongly increases (fig. S5).

The plasmonic drawbridge: Reversible switching between capacitive and conductive coupling

By further increasing the thickness of the Ag shells and by applying sufficient step potentials, the coupling mechanism for nanoparticle dimers was reversibly switched between capacitive and conductive coupling (Fig. 3). TEM imaging revealed the detailed structure of Au/Ag bridged dimers (Fig. 3A). Under electrochemical potential control, the shell can be actively tuned between semiconducting AgCl and highly conductive metallic Ag. It is expected that as the advancing metallic surfaces of the nanoparticles approach contact, electron tunneling provides a charge transfer pathway between nanoparticles (16, 23). Electric contact of the two Au nanoparticles established through the Ag metal bridge results in an oscillating current between

the nanoparticles and multiple corresponding charge transfer plasmon modes (14, 38). Simulated and experimental spectra both reveal the emergence of a new longitudinal screened bonding (SB) dipolar plasmon mode (Fig. 3B). The SB mode is a longitudinal charge transfer plasmon mode characterized by a significant charge transfer between Ag shells and by a weak quadrupolar polarization of the cores (14–17, 39).

A series of scattering spectra of an individual Au/Ag dimer shows broad tuning of the plasmon modes in response to repeated formation and removal of the conductive bridge between the Au cores (Fig. 3C). The transition from capacitive to conductive coupling at negative bias is clearly visible with the emergence of significantly brighter shell-dominated SB and T modes (Fig. 3C). By then applying a positive bias, conductive coupling was broken as the shell composition was switched to AgCl. This event is visible in the scattering spectra with the re-emergence of the core-dominated LB and T modes. This plasmonic "drawbridge" effect was reversible over at least 30 full cycles and was not observed to disappear or degrade. This effect was observed for all dimers studied and was clearly visible by eye in dark-field microscopy through changes in both color and intensity (figs. S6 and S7). We also observed that the chloridation reaction (Ag → AgCl) under oxidizing potentials causes much faster spectral changes than the reduction reaction (AgCl → Ag) under reducing potentials (video S1). The asymmetric response rate may be due to sluggish Ag reduction kinetics, as recently reported for the reduction of Ag ions from solution (40).

As in the thin-shell case, simulations revealed that the Ag shell dominates the optical response in the reduced state, whereas the Au cores
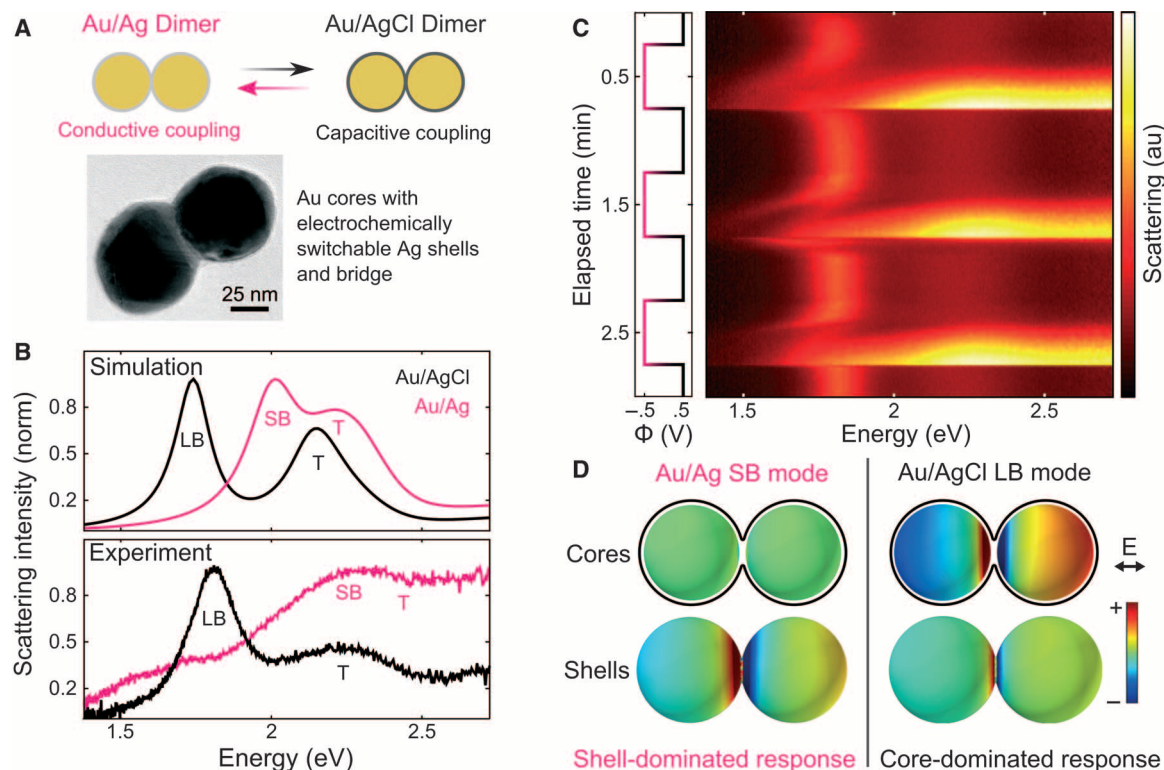

Fig. 3. Reversible electrochemical tuning of a dimer between capacitive and conductive coupling. (**A**) Overlapping shells on Au dimers were switched between Ag and AgCl to create a switch between capacitive and conductive coupling. TEM image shows an Au dimer enveloped by Ag shell. (**B**) Simulated and experimental scattering spectra show a drastic optical response to switching the plasmon coupling mechanism. (**C**) Series of scattering spectra during step potential application to switch shell composition. (**D**) Surface charge density plots of shell and core surfaces for SB and LB modes. Charge plots were calculated at 2.0 eV for the SB mode and at 1.67 eV for the LB mode.

dominate in the oxidized state. Charge density plots demonstrate the relative contributions of the shells and cores to the two longitudinal modes, SB and LB (Fig. 3D). For the SB mode, charge density on Ag shell surfaces is more than 10 times greater than that on Au core surfaces (Fig. 3D, left). For the LB mode, charges are distributed primarily on the Au core surfaces, with no current flowing between the two Au cores (Fig. 3D, right). Again, the strong electric fields induce a visible polarization response in the AgCl shells near the gap (Fig. 3D, bottom right). Charge density plots of the T modes of both shell states revealed the same relative contribution of shells and cores to the optical response as the longitudinal modes (fig. S8).

By decreasing the size of the Au cores to 40 nm and lowering the reductive overpotential, we characterized the spectral evolution of the pure CTP mode in addition to the SB and T modes for an individual dimer (Fig. 4A). FEM simulations correctly predicted that, given the same Ag shell thickness and core separation distance, the CTP resonance energy blue shifts with decreasing Au core size as a result of a reduction in coupling between the Ag shells (fig. S9). In addition, by lowering the Ag/AgCl redox overpotentials, the rates of the chloridation and reduction reactions were decreased (41). The AgCl shell was slowly reduced to Ag

by applying a step potential slightly more negative than the equilibrium potential (−0.22 V versus Pt). Because of the smaller dimer, the pure CTP mode remained within the spectral detection range of our silicon photodetector. We clearly observed the formation of the SB mode, compared with the LB mode, at higher energy. The formation of the SB mode at roughly 42 s indicates the formation of a conductive pathway between the two lobes of the bridged dimer. As the shell is further converted into Ag, an increase in coupling between the Ag shells leads to a red shift of the CTP and SB modes (Fig. 4A). Then, by switching to an oxidizing potential, the Ag shell was converted back to AgCl. As demonstrated for the larger bridged dimer (Fig. 3), the charge density distribution for the longitudinal modes is dominated by the Ag shells. The calculated charge density plot of the CTP mode shows a characteristic dipolar charge distribution on the Ag shell surface, with charge strongly localized near the gap region (Fig. 4A, inset).

Detailed mechanistic information can be extracted from the slow evolution of the scattering spectrum during electrochemical conversion of the bridging shell. Soon after the application of a reduction potential, a rapid red shift occurred along with the disappearance of the core-dominated LB and T modes (Fig. 4A, bottom). This transition
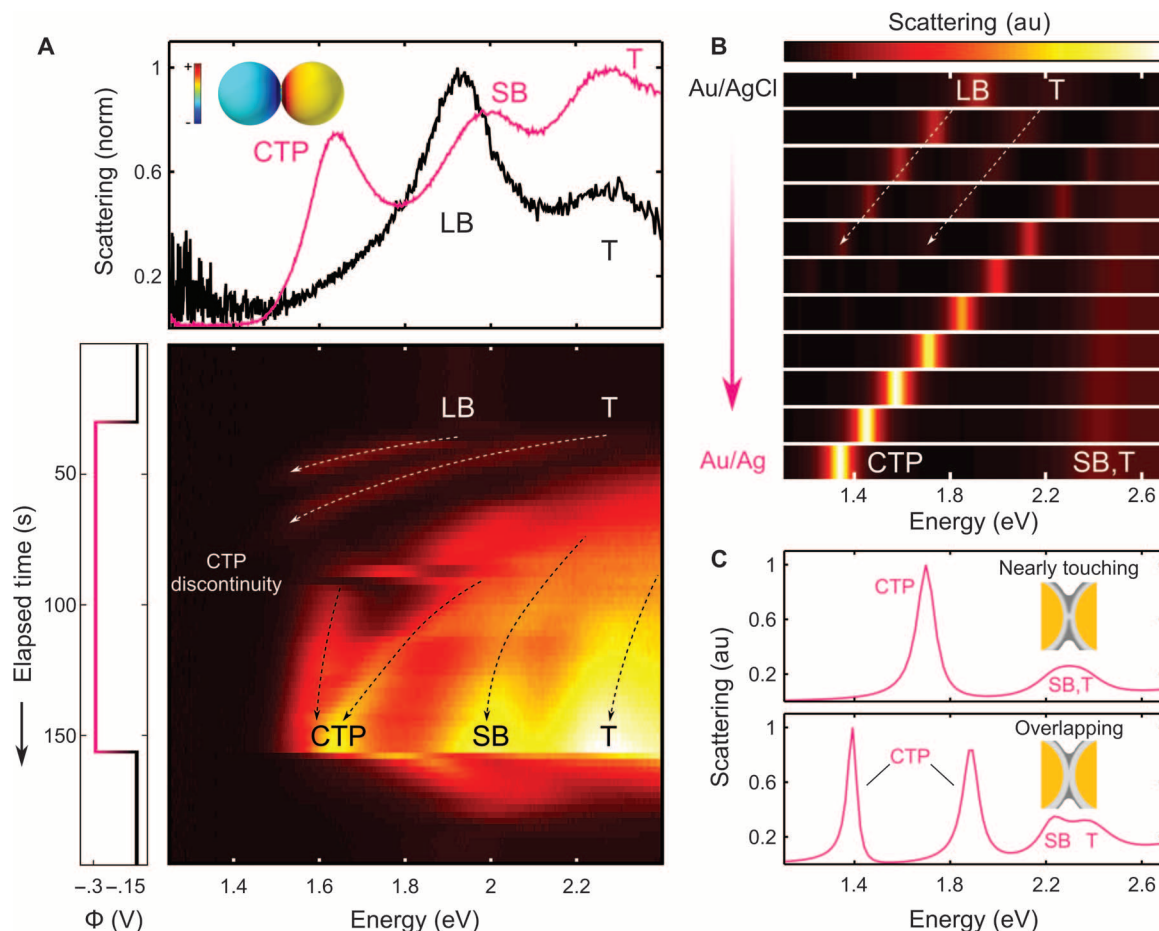

Fig. 4. Dynamic evolution of the CTP mode using 40-nm Au cores and decreased overpotential. (**A**) Experimental static (top) and dynamic (bottom) scattering observations of slow bridging during the conversion between AgCl and Ag shells for an individual Au/Ag dimer with 40-nm Au cores at −0.22 V. (Inset) Surface charge density plot of the outer Ag shell surface for the CTP mode (calculated at 1.35 eV). (**B**) Predicted spectral evolution with electrochemical shell conversion from pure AgCl to pure Ag using isotropic dielectric mixing approximation. (**C**) CTP mode splitting in simulations using bridged concentric Ag growth mechanism at the point of Ag shell overlap (full evolution in fig. S10B).

corresponds to the increasing real part of the dielectric function of the shell with increasing Ag content and the corresponding dominance of the shell-dominated plasmon resonance modes. Later, the CTP and SB modes emerged at much higher energy than the LB mode because of the formation of a conductive pathway, as mentioned previously. With increasing Ag content, the CTP and SB modes grew in intensity and red shifted until the shells reached full Ag content. The red shifts of the capacitively coupled modes, especially their decreasing spectral weight, and the general evolution of the conductively coupled modes with increasing Ag content, can be understood from full wave simulations using isotropic dielectric mixing of Ag and AgCl (Fig. 4B). With increasing Ag content (Fig. 4B, from top to bottom), the core-dominated LB and T modes gradually red shift and fade away, just as observed in single-particle spectra. The calculated scattering spectra also show the same high-energy origin and red shift of the CTP mode with increasing Ag content. At the present size, however, the SB and T modes lie at very similar resonance energies in the simulated spectra, precluding a clear analysis of their evolution.

Estimates of the electrochemical reaction rates through the full experimental spectral response are possible by assuming idealized spherical cores, 3-nm conformal overlapping shells, and full conversion of shells between AgCl and Ag. With these parameters, we calculate that AgCl was converted into Ag at a rate of ~2200 atoms/s, whereas in the oxidation step, Ag was converted into AgCl at ~8700 atoms/s. Even at a low reaction overpotential, the conversion from Ag into AgCl was still about four times faster than the reverse process under our experimental conditions. The asymmetric response rates can be explained in terms of sluggish Ag reduction kinetics, as recently reported for the reduction of Ag ions from solution (40) or differences in active ion transport rates (42).

The experimental spectral evolution at the onset of conductive coupling indicates a short-lived intermediate (labeled CTP discontinuity in Fig. 4A) that is not predicted by the isotropic dielectric mixing model. At roughly 75 s in Fig. 4A, a new low-energy spectral feature briefly developed at 1.7 eV. For three sequential exposures (7.5 s), only one low-energy peak was visible but was abruptly replaced by the return of two peaks. With a further increase in the Ag content of the shells, the two peaks gradually converged to form the CTP mode. Clearly, the isotropic dielectric mixing model of Fig. 4B cannot address this evolution near the point of contact. Short-lived intermediates in the spectral evolution were also observed in other dimer bridging experiments. These results are similar to previous investigations of the fusion of small Ag nanoparticles using electron energy loss spectroscopy, which showed evidence of splitting of the pure CTP mode near the point of physical contact (39).

Further simulations with variations in bridging geometry allow for an insight into these intermediates. We explored alternate Ag shell growth mechanisms, including concentric sphere growth with and without a thin metal bridge (fig. S10 and Materials and Methods). In short, we found that, in the case of bridged concentric sphere growth, the CTP mode splits at the point of overlap for the Ag shells (Fig. 4C). In addition to the aforementioned experimental observation upon nanoparticle contact and observed splitting in our simulations, full quantum mechanical calculations of bridged dimers have also shown weak splitting of the CTP mode near the point of physical contact (15, 43). Because the system dimensions and specific geometry of the gap play a major role in the formation and evolution of charge transfer plasmons

(14–16, 19, 20), we include the full evolution of each bridge model investigated in fig. S10. On the basis of these simulation results of our dielectric mixing and concentric shell growth models, we must conclude that the experimental system is best described by a combination of these two extreme cases.

Comparing the experimental and simulated scattering spectra for the bridged dimers, two remarks are in order. First, assuming the same shell thickness for both redox states, the tunneling conductance of Ag shells causes the SB mode to have a higher resonance energy than the LB mode. Experimentally, the resonance energy difference between LB and SB modes varied from structure to structure. Along with a likely dependence on individual gap geometry, the shell thickness also plays an important role. With increasing shell thickness, the LB mode always red shifts; the SB mode initially red shifts because of increased coupling strength, but then blue shifts because of increasing tunneling current (fig. S11). Hence, for identical core structures, larger differences between LB and SB resonance energies correspond to increased shell overlap. In the cases of isotropic dielectric mixing simulations (Fig. 4B) and concentric sphere growth simulations (Fig. 4C and fig. S10), small differences in plasmon resonance energies are observed between simulated and experimental scattering spectra. We attribute these differences to the known variations in nanoparticle and bridge morphology (Fig. 3A and fig. S3), which are not accounted for in the idealized geometries of simulations. Finally, we note that no illumination dependence was observed in bulk cyclic voltammograms or initial Ag shell deposition (fig. S12).

CONCLUSIONS

Using Ag redox chemistry, we demonstrated fully reversible active control of plasmon resonances in both isolated and interacting plasmonic nanoparticles. For dimers, the plasmon shifts were particularly large because our approach allowed us to fill the junction and to introduce or remove conductive coupling between the nanoparticles. Our results show that electrochemical modification of plasmonic nanoparticles allows predictable, reversible, and fully controllable modulation of the intensity, line shape, and color of both simple and complex nanostructures. These results constitute the first observation of reversible CTP formation in nanoparticle dimers. Our study also includes the first continuous measurements of the evolution of the SB and CTP modes during the bridging process. In addition, by comparing experimental spectral evolution with various simulation geometries, it is possible to extract details on the exact mechanism of the bridging geometry. In addition to providing a valuable model system for investigating the transitions between capacitive and conductive coupling, these results also pave the way for new research opportunities, such as more detailed studies of controlled narrow plasmonic gap effects, electrochemical potential–directed nanoparticle growth, electrochemical alloying, or layer-by-layer active plasmonics.

MATERIALS AND METHODS

Dimer preparation
Au nanoparticle dimers were prepared using a nonspecific aggregation method and electrophoretic enrichment, as described previously (36). Five hundred microliters of stock citrate-stabilized 50-nm Au colloids

Byers *et al. Sci. Adv.* 2015;1:e1500988   4 December 2015

6 of 9

(BBI Solutions) was washed once with Millipore filtered deionized water and concentrated to a volume of 50 μl by centrifugation at 1400 relative centrifugal force for 5 min. Two hundred microliters of acetonitrile was added to the suspension and stirred for 30 min. Five microliters of 10 mM 11-mercaptoundecanoic acid (11-MUA; Sigma-Aldrich) was added, followed by 30 min of stirring. The solution was centrifuged, and the supernatant was removed. Sedimented nanoparticles and aggregates were resuspended in 500 μl of Millipore filtered deionized water, washed again, and concentrated to a volume of 50 μl. Ten microliters of 40% (w/v) aqueous solution was added to facilitate horizontal gel electrophoretic separation of aggregates consisting of various numbers of nanoparticles. Samples were electrophoretically separated in 1% agarose gel at 135 V for 30 min in 0.5× tris-acetate-EDTA buffer. The second band was manually removed with a razor blade, and aggregates and single nanoparticles in the removed gel were removed using a published electroelution method at 250 V (44). Extracted nanoparticles and aggregates were centrifuged, washed, and concentrated for deposition. TEM analysis showed that the resulting solution contained 23% dimers with gap widths ranging from 1 to 5 nm. TEM images of single nanoparticles in prepared dimer solutions were analyzed to find the average cross-sectional area, using an algorithm adapted from Gontard *et al.* (45). Identical procedures were followed using 40-nm Au colloids (BBI Solutions) to produce smaller dimers.

Electrochemical cell preparation

Single nanoparticles and dimers were drop cast onto indium tin oxide (ITO)–coated coverslips and washed to remove excess nanoparticles. 11-MUA was removed from the nanoparticles by soaking in a $NH_4OH/H_2O_2/H_2O$ solution (volume ratio 2.3:1:38.6) for 10 min at 40°C (46). Samples were then rinsed thoroughly with water and dried with nitrogen gas. Optically transparent sealed thin electrochemical cells were constructed using the hybrid ITO Au nanoparticle substrate as a working electrode. An insulated 0.05-mm-diameter platinum wire was used as a quasi-reference electrode (A-M Systems). The counter electrode was formed by either a clean platinum or an anodically chloridized Ag wire (Sigma Aldrich). All electrolytes were prepared using American Chemical Society–grade reagents (Sigma Aldrich). In the case of the Ag/AgCl counter electrode, Ag chloro-complexes were dissolved into the NaCl host electrolyte. Ag was electrodeposited onto bare Au nanoparticles and dimers. The Ag/AgCl reaction was also characterized by comparison to an Ag/AgCl reference electrode (fig. S13).

Dark-field scattering measurements

Single-particle and single-dimer spectra were collected on a custom instrument described previously (7). In short, spectra from individual scatterers were collected on an inverted dark-field microscope (Zeiss Axio Observer m1, with oil immersion dark-field condenser and oil immersion Zeiss Plan-Achromat 63×, numerical aperture of 0.7 to 1.4). Light was directed to an Acton SpectraPro 2150i imaging spectrograph mounted atop a programmatically controlled linear translation stage (Newport, model LTA-HL). A control program (Labview, 2011) linked incoming spectra with an electrochemical workstation (CH Instruments, model 630D) allowing time/potential-correlated dynamic spectroelectrochemcial measurements. A nonlinear least-squares fitting algorithm (Matlab 2013a) was used to fit single- and double-Lorentzian curves to single-nanoparticle and dimer scattering spectra, respectively.

Au nanoparticle and dimer TEM sample preparation

Ten microliters of an aqueous suspension containing 11-MUA–coated 50-nm-diameter Au nanoparticles and dimers was drop cast onto a 300-mesh Cu TEM grid precoated with lacey carbon films from Pacific Grid Tech (Cu-300LD) and dried in air.

Au/Ag core-shell nanoparticle and dimer TEM sample preparation

Two microliters of an aqueous suspension containing 11-MUA–coated 50-nm-diameter Au nanoparticles and dimers was drop cast onto a clean ITO-coated glass coverslip (ECI). 11-MUA was removed from the nanoparticles by soaking in a $NH_4OH/H_2O_2/H_2O$ solution (volume ratio 1:2.3:38.6) for 10 min at 40°C (46). Au nanoparticles and dimers were electrochemically coated in Ag in the spectroelectrochemical cell. After disassembly of the spectroelectrochemical cell, Au-Ag core-shell nanoparticles and dimers were removed from their ITO support by sonication into 2 mM sodium citrate solution. Ten microliters of the suspension was dried onto a 300-mesh Cu ultrathin TEM grid precoated with lacey carbon films. Excess citrate was rinsed with running Milli-Q filtered deionized water, and grids were dried with dry nitrogen.

Au nanoparticle and dimer scanning electron microscopy sample preparation

Two microliters of an aqueous suspension containing 11-MUA–coated 50-nm-diameter Au nanoparticles and dimers was drop cast onto a clean ITO-coated glass coverslip (ECI). 11-MUA was removed from the nanoparticles by soaking in a $H_2O_2/NH_4OH/H_2O$ solution (volume ratio 1:2.3:38.6) for 10 min at 40°C (46). Au nanoparticles and dimers were cycled 50 times between −0.5 and 0.5 V in 100 mM NaCl electrolyte with no Ag present. The spectroelectrochemical cell was disassembled, and the ITO working electrode was rinsed with running Milli-Q filtered deionized water and dried with dry nitrogen.

Au/Ag nanoparticle and dimer scanning electron microscopy sample preparation

Two microliters of an aqueous suspension containing 11-MUA–coated 50-nm-diameter Au nanoparticles and dimers was drop cast onto a clean ITO-coated glass coverslip (ECI). 11-MUA was removed from the nanoparticles by soaking in a $NH_4OH/H_2O_2/H_2O$ solution (volume ratio 1:2.3:38.6) for 10 min at 40°C (46). Au nanoparticles and dimers were electrochemically coated in Ag. The spectroelectrochemical cell was disassembled, and the ITO working electrode was rinsed with running Milli-Q filtered deionized water and dried with dry nitrogen.

Scanning electron microscopy methods

Scanning electron micrographs were taken with an FEI Quanta 650 FEG ESEM with a beam energy of 30.0 kV. All images were taken directly from the ITO working electrode after the sample preparation.

TEM methods

TEM images were taken with a JEOL-2100F field emission electron microscope operated at 200 kV. HAADF-STEM images were taken using a Gatan 806 detector. EDS was performed using an Oxford Instruments EDS INCA x-sight detector, and data were collected using the INCA software. Raw data from STEM-EDS were processed using HyperSpy (open source, available at www.hyperspy.org) multidimensional data analysis toolbox version 0.8. EDS elemental maps were produced from

background-subtracted Au-Mα_1 (2.12 keV) and Ag-Lα_1 (2.98 keV) x-ray peaks (47) using FIJI (open source, available at http://Fiji.sc/Fiji).

Simulation methods

Modeling and simulations were performed using the FEM (COMSOL Multiphysics) with the same detection geometry as adopted experimentally (fig. S14). An effective medium approximation was used under a homogenous refractive index as

$$n = \sqrt{\frac{n_{\text{water}}^2 + n_{\text{ITO}}^2}{2}}$$

where $n_{\text{water}} = 1.33$ and $n_{\text{ITO}} = 1.97$. The Au dimer structure consisted of two spheres with a 48-nm center-to-center distance as measured by TEM (fig. S3). Because of the nonuniform sizes of nanoparticles (fig. S2), a 44-nm-diameter Au dimer is adopted in Fig. 2 to match the experiments, whereas Fig. 3 uses 45-nm-diameter Au dimers. The core-shell system investigated was an Au core–Ag$_\alpha$ AgCl$_{1-\alpha}$–shell system with shell thicknesses varying from 0 nm (pure Au dimer) to 1.6 nm (overlapping shell case with 0.4 nm radius rounding). The 1.5-nm shell case corresponds to the touching geometry. To show the evolution of modes with increasing Ag content of the bridged structure, we adopted the real experimental conditions in Fig. 4 and fig. S10 (water medium, ITO substrate, and 40-nm-diameter Au cores). The dielectric functions of Au and Ag were taken from the work of Johnson and Christy (48), which has been widely used for Au and Ag nanomaterials. The refractive index of AgCl was $n = 2.02$, as taken from White and Straley (33) and Tilton et al. (34). Finally, an averaging procedure over a nonnormal incident (56.4°) light cone was performed so that the simulation results can be directly compared with dark-field scattering spectra. With increasing shell thickness (Ag or AgCl), the LB mode strongly red shifts (fig. S4) as observed in the experiments (Fig. 2). In terms of nanoparticle coupling, an increasing shell thickness decreases the gap width, resulting in larger capacitive coupling. The growth mechanism of Ag content inside the shell was studied under two hypotheses: (i) isotropic dielectric mixing of Ag and AgCl (Fig. 4B) under the Maxwell-Garnett medium approximation method (8); and (ii) concentric spherical growth of Ag around core surfaces (42, 49) (Fig. 4C and fig. S10). Because a bridge connecting the Au cores may be formed when the Ag content increases (22, 23), we consider three different cases in terms of bridge growth rate: (i) no bridge at all unless Ag shells touch; (ii) a thin bridge is formed before the Ag shells overlap ($^1/_{10}$ the width of the total bridge); and (iii) the Ag bridge has the same growth rate as that of Ag shells. As seen in Fig. 4B, all modes red shift with increasing Ag content under the isotropic dielectric mixing hypothesis. Specifically, the LB and T modes of Au/AgCl gradually red shift and disappear because they are core-dominant modes. Meanwhile, new modes dominated by Ag shells (that is, T, SB, and CTP) appear and red shift with increasing Ag content. For the concentric spherical growth hypothesis, on the other hand, the evolution shows a completely different behavior (fig. S10). When the bridge growth rate is much smaller than that of Ag shells (fig. S10A, no bridge case; Fig. 4C and fig. S10B, constant ratio thin bridge case), the concentric growth dominates the optical response before touching, and the LB mode red shifts because of the increased coupling between the Ag shells. Upon shell overlap, an abrupt discontinuity appears, and the CTP mode splits into two resonances (Fig. 4C and boxed spectra in fig. S10B), consistent with what has been observed previously (15, 39, 43). After touching, the SB and CTP modes blue shift as a result of the increase in bridge conductance (50). When the bridge growth rate is com-

parable to that of Ag shells (same growth rate; fig. S10C), the increase in bridge conductance dominates throughout the entire spectral evolution, resulting in clear blue shifts for LB and T modes for small Ag shells, as well as T, SB, and CTP modes for touching nanoparticles.

SUPPLEMENTARY MATERIALS

Supplementary material for this article is available at http://advances.sciencemag.org/cgi/content/full/1/11/e1500988/DC1

Fig. S1. EDS spectrum and line scan profile of single Au/Ag nanoparticle.
Fig. S2. Surface charge plots for an Au/Ag core-shell nanoparticle.
Fig. S3. Transmission electron micrographs showing the native structure of gold nanoparticle dimers and size analysis of single gold nanoparticles.
Fig. S4. Surface charge plots for the T mode for thin-shelled dimers.
Fig. S5. Effects of increasing shell thickness on Ag and AgCl shells.
Fig. S6. Digital color images taken with an SLR (single-lens reflex) camera at microscope eyepiece during initial electrodeposition.
Fig. S7. Color images of Au/Ag single particles and dimers under oxidizing and reducing conditions.
Fig. S8. Charge density maps of T modes for both shell states for bridged dimers.
Fig. S9. Effects of varying Au core size on Au/Ag bridged dimers.
Fig. S10. Mode evolution with increasing Ag content under concentric spherical growth hypotheses.
Fig. S11. Evolution of the SB mode with increasing Ag shell thickness.
Fig. S12. Cyclic voltammogram with and without illumination of the working electrode.
Fig. S13. Electrochemical characterization of the Au/Ag surface reaction.
Fig. S14. Diagram showing sample geometry used in FEM simulations.
Video S1. Effects of redox tuning for a conductively bridged dimer.

REFERENCES AND NOTES

1. J. Berthelot, A. Bouhelier, C. Huang, J. Margueritat, G. Colas-des-Francs, E. Finot, J.-C. Weeber, A. Dereux, S. Kostcheev, H. Ibn El Ahrach, A.-L. Baudrion, J. Plain, R. Bachelot, P. Royer, G. P. Wiederrecht, Tuning of an optical dimer nanoantenna by electrically controlling its load impedance. *Nano Lett.* **9**, 3914–3921 (2009).
2. M. I. Lapsley, A. Shahravan, Q. Hao, B. K. Juluri, S. Giardinelli, M. Lu, Y. Zhao, I.-K. Chiang, T. Matsoukas, T. J. Huang, Shifts in plasmon resonance due to charging of a nanodisk array in argon plasma. *Appl. Phys. Lett.* **100**, 101903 (2012).
3. C. Novo, A. M. Funston, P. Mulvaney, Direct observation of chemical reactions on single gold nanocrystals using surface plasmon spectroscopy. *Nat. Nanotechnol.* **3**, 598–602 (2008).
4. A. B. Dahlin, R. Zahn, J. Vörös, Nanoplasmonic sensing of metal–halide complex formation and the electric double layer capacitor. *Nanoscale* **4**, 2339–2351 (2012).
5. R. MacKenzie, C. Fraschina, B. Dielacher, T. Sannomiy, A. B. Dahlin, J. Vörös, Simultaneous electrical and plasmonic monitoring of potential induced ion adsorption on metal nanowire arrays. *Nanoscale* **5**, 4966–4975 (2013).
6. S. K. Dondapati, M. Ludemann, R. Müller, S. Schwieger, A. Schwemer, B. Händel, D. Kwiatkowski, M. Djiango, E. Runge, T. A. Klar, Voltage-induced adsorbate damping of single gold nanorod plasmons in aqueous solution. *Nano Lett.* **12**, 1247–1252 (2012).
7. C. P. Byers, B. S. Hoener, W.-S. Chang, M. Yorulmaz, S. Link, C. F. Landes, Single-particle spectroscopy reveals heterogeneity in electrochemical tuning of the localized surface plasmon. *J. Phys. Chem. B* **118**, 14047–14055 (2014).
8. C. Novo, A. M. Funston, A. K. Gooding, P. Mulvaney, Electrochemical charging of single gold nanorods. *J. Am. Chem. Soc.* **131**, 14664–14666 (2009).
9. T. Sannomiya, H. Dermutz, C. Hafner, J. Vörös, A. B. Dahlin, Electrochemistry on a localized surface plasmon resonance sensor. *Langmuir* **26**, 7619–7626 (2010).
10. M. Chirea, S. S. E. Collins, X. Wei, P. Mulvaney, Spectroelectrochemistry of silver deposition on single gold nanocrystals. *J. Phys. Chem. Lett.* **5**, 4331–4335 (2014).
11. T. Miyazaki, R. Hasegawa, H. Yamaguchi, H. Oh-oka, H. Nagato, I. Amemiya, S. Uchikoga, Electrical control of plasmon resonance of gold nanoparticles using electrochemical oxidation. *J. Phys. Chem. C* **113**, 8484–8490 (2009).
12. L. Gao, Y. Zhang, H. Zhang, S. Doshay, X. Xie, H. Luo, D. Shah, Y. Shi, S. Xu, H. Fang, J. A. Fan, P. Nordlander, Y. Huang, J. A. Rogers, Optics and nonlinear buckling mechanics in large-area, highly stretchable arrays of plasmonic nanostructures. *ACS Nano* **9**, 5968–5975 (2015).
13. F. Huang, J. J. Baumberg, Actively tuned plasmons on elastomerically driven Au nanoparticle dimers. *Nano Lett.* **10**, 1787–1792 (2010).

14. O. Pérez-González, N. Zabala, A. G. Borisov, N. J. Halas, P. Nordlander, J. Aizpurua, Optical spectroscopy of conductive junctions in plasmonic cavities. *Nano Lett.* **10**, 3090–3095 (2010).

15. R. Esteban, A. G. Borisov, P. Nordlander, J. Aizpurua, Bridging quantum and classical plasmonics with a quantum-corrected model. *Nat. Commun.* **3**, 825 (2012).

16. K. J. Savage, M. M. Hawkeye, R. Esteban, A. G. Borisov, J. Aizpurua, J. J. Baumberg, Revealing the quantum regime in tunnelling plasmonics. *Nature* **491**, 574–577 (2012).

17. T. V. Teperik, P. Nordlander, J. Aizpurua, A. G. Borisov, Robust subnanometric plasmon ruler by rescaling of the nonlocal optical response. *Phys. Rev. Lett.* **110**, 263901 (2013).

18. C. Ciracì, R. T. Hill, J. J. Mock, Y. Urzhumov, A. I. Fernández-Domínguez, S. A. Maier, J. B. Pendry, A. Chilkoti, D. R. Smith, Probing the ultimate limits of plasmonic enhancement. *Science* **337**, 1072–1074 (2012).

19. R. Esteban, G. Aguirregabiria, A. G. Borisov, Y. M. Wang, P. Nordlander, G. W. Bryant, J. Aizpurua, The morphology of narrow gaps modifies the plasmonic response. *ACS Photonics* **2**, 295–305 (2015).

20. R. Esteban, A. Zugarramurdi, P. Zhang, P. Nordlander, F. J. García-Vidal, A. G. Borisov, J. Aizpurua, A classical treatment of optical tunneling in plasmonic gaps: Extending the quantum corrected model to practical situations. *Faraday Discuss.* **178**, 151–183 (2015).

21. F. Wen, Y. Zhang, S. Gottheim, N. S. King, Y. Zhang, P. Nordlander, N. J. Halas, Charge transfer plasmons: Optical frequency conductances and tunable infrared resonances. *ACS Nano* **9**, 6428–6435 (2015).

22. L. O. Herrmann, V. K. Valev, C. Tserkezis, J. S. Barnard, S. Kasera, O. A. Scherman, J. Aizpurua, J. J. Baumberg, Threading plasmonic nanoparticle strings with light. *Nat. Commun.* **5**, 4568 (2014).

23. T. Hartling, Y. Alaverdyan, A. Hille, M. T. Wenzel, M. Käll, L. M. Eng, Optically controlled interparticle distance tuning and welding of single gold nanoparticle pairs by photochemical metal deposition. *Opt. Express* **16**, 12362–12371 (2008).

24. T. Kim, K. Lee, M.-S. Gong, S.-W. Joo, Control of gold nanoparticle aggregates by manipulation of interparticle interaction. *Langmuir* **21**, 9524–9528 (2005).

25. D.-K. Lim, K.-S. Jeon, H. M. Kim, J.-M. Nam, Y. D. Suh, Nanogap-engineerable Raman-active nanodumbbells for single-molecule detection. *Nat. Mater.* **9**, 60–67 (2010).

26. J. J. Fritz, Thermodynamic properties of chloro-complexes of silver chloride in aqueous solution. *J. Solut. Chem.* **14**, 865–879 (1985).

27. T. Ung, M. Giersig, D. Dunstan, P. Mulvaney, Spectroelectrochemistry of colloidal silver. *Langmuir* **13**, 1773–1782 (1997).

28. Y. Hamasaki, N. Nakashima, Y. Niidome, Effects of anions on electrochemical reactions of silver shells on gold nanorods. *J. Phys. Chem. C* **117**, 2521–2530 (2013).

29. Y. Okuno, K. Nishioka, A. Kiya, N. Nakashima, A. Ishibashi, Y. Niidome, Uniform and controllable preparation of Au-Ag core-shell nanorods using anisotropic silver shell formation on gold nanorods. *Nanoscale* **2**, 1489–1493 (2010).

30. K. Park, L. F. Drummy, R. A. Vaia, Ag shell morphology on Au nanorod core: Role of Ag precursor complex. *J. Mater. Chem.* **21**, 15608–15618 (2011).

31. S. Gómez-Graña, B. Goris, T. Altantzis, C. Fernández-López, E. Carbó-Argibay, A. Guerrero-Martínez, N. Almora-Barrios, N. López, I. Pastoriza-Santos, J. Pérez-Juste, S. Bals, G. Van Tendeloo, L. M. Liz-Marzán, Au@Ag nanoparticles: Halides stabilize {100} facets. *J. Phys. Chem. Lett.* **4**, 2209–2216 (2013).

32. Y. Fang, W. Wang, X. Wo, Y. Luo, S. Yin, Y. Wang, X. Shan, N. Tao, Plasmonic imaging of electrochemical oxidation of single nanoparticles. *J. Am. Chem. Soc.* **136**, 12584–12587 (2014).

33. J. J. White, J. W. Straley, Optical properties of silver chloride. *J. Opt. Soc. Am.* **58**, 759–763 (1968).

34. L. W. Tilton, E. K. Plyler, R. E. Stephens, Refractive index of silver chloride for visible and infra-red radiant energy. *J. Opt. Soc. Am.* **40**, 540–543 (1950).

35. S. Bidault, A. Polman, Water-based assembly and purification of plasmon-coupled gold nanoparticle dimers and trimers. *Int. J. Opt.* **2012**, 387274 (2012).

36. D. Huang, C. P. Byers, L.-Y. Wang, A. Hoggard, B. Hoener, S. Dominguez-Medina, S. Chen, W.-S. Chang, C. F. Landes, S. Link, Photoluminescence of a plasmonic molecule. *ACS Nano* **9**, 7072–7079 (2015).

37. P. K. Jain, W. Huang, M. A. El-Sayed, On the universal scaling behavior of the distance decay of plasmon coupling in metal nanoparticle pairs: A plasmon ruler equation. *Nano Lett.* **7**, 2080–2088 (2007).

38. L. Liu, Y. Wang, Z. Fang, K. Zhao, Plasmon hybridization model generalized to conductively bridged nanoparticle dimers. *J. Chem. Phys.* **139**, 064310 (2013).

39. J. A. Scholl, A. García-Etxarri, A. L. Koh, J. A. Dionne, Observation of quantum tunneling between two plasmonic nanoparticles. *Nano Lett.* **13**, 564–569 (2013).

40. C. M. Hill, R. Bennett, C. Zhou, S. Street, J. Zheng, S. Pan, Single Ag nanoparticle spectro-electrochemistry via dark-field scattering and fluorescence microscopies. *J. Phys. Chem. C* **119**, 6760–6768 (2015).

41. A. J. Bard, L. R. Faulkner, *Electrochemical Methods, Fundamentals and Applications* (John Wiley and Sons, New York, ed. 2, 2001).

42. T. Katan, S. Szpak, D. N. Bennion, Silver/silver chloride electrode: Reaction paths on discharge. *J. Electrochem. Soc.* **120**, 883–888 (1973).

43. D. C. Marinica, A. K. Kazansky, P. Nordlander, J. Aizpurua, A. G. Borisov, Quantum plasmonics: Nonlinear effects in the field enhancement of a plasmonic nanoparticle dimer. *Nano Lett.* **12**, 1333–1339 (2012).

44. B. M. Reinhard, S. Sheikholeslami, A. Mastroianni, A. P. Alivisatos, J. Liphardt, Use of plasmon coupling to reveal the dynamics of DNA bending and cleavage by single EcoRV restriction enzymes. *Proc. Natl. Acad. Sci. U.S.A.* **104**, 2667–2672 (2007).

45. L. C. Gontard, D. Ozkaya, R. E. Dunin-Borkowski, A simple algorithm for measuring particle size distributions on an uneven background from TEM images. *Ultramicroscopy* **111**, 101–106 (2011).

46. D. J. Kim, R. Pitchimani, D. E. Snow, L. J. Hope-Weeks, A simple method for the removal of thiols on gold surfaces using an $NH_4OH–H_2O_2–H_2O$ solution. *Scanning* **30**, 118–122 (2008).

47. D. Rossouw, P. Burdet, F. de la Peña, C. Ducati, B. R. Knappett, A. E. H. Wheatley, P. A. Midgley, Multicomponent signal unmixing from nanoheterostructures: Overcoming the traditional challenges of nanoscale x-ray analysis via machine learning. *Nano Lett.* **15**, 2716–2720 (2015).

48. P. B. Johnson, R. W. Christy, Optical constants of the noble metals. *Phys. Rev. B* **6**, 4370 (1972).

49. D. M. Mott, D. T. N. Anh, P. Singh, C. Shankar, S. Maenosono, Electronic transfer as a route to increase the chemical stability in gold and silver core–shell nanoparticles. *Adv. Colloid Interface Sci.* **185–186**, 14–33 (2012).

50. V. Kulkarni, A. Manjavacas, Quantum effects in charge transfer plasmons. *ACS Photonics* **2**, 987–992 (2015).

Author/s:
Byers, CP; Zhang, H; Swearer, DF; Yorulmaz, M; Hoener, BS; Huang, D; Hoggard, A;
Chang, W-S; Mulvaney, P; Ringe, E; Halas, NJ; Nordlander, P; Link, S; Landes, CF

Title:
From tunable core-shell nanoparticles to plasmonic drawbridges: Active control of
nanoparticle optical properties

Date:
2015-12-01

Persistent Link:
http://hdl.handle.net/11343/129674

File Description:
Published version
License: